



Inferring Direction and Orientation from Polarized Signals: Feasibility and Bounds

Downloaded from: <https://research.chalmers.se>, 2024-11-05 11:27 UTC

Citation for the original published paper (version of record):

Ibrahim, E., Chen, H., Ye, Z. et al (2024). Inferring Direction and Orientation from Polarized Signals: Feasibility and Bounds. *IEEE Open Journal of the Communications Society*, 5: 6033-6047.
<http://dx.doi.org/10.1109/OJCOMS.2024.3462689>

N.B. When citing this work, cite the original published paper.

© 2024 IEEE. Personal use of this material is permitted. Permission from IEEE must be obtained for all other uses, in any current or future media, including reprinting/republishing this material for advertising or promotional purposes, or reuse of any copyrighted component of this work in other works.

Inferring Direction and Orientation From Polarized Signals: Feasibility and Bounds

EMAD IBRAHIM¹, HUI CHEN² (Member, IEEE), ZI YE¹, REZA GHAZALIAN³,
HYOWON KIM⁴ (Member, IEEE), RICKARD NILSSON¹, HENK WYMEERSCH² (Fellow, IEEE),
AND JAAP VAN DE BEEK¹ (Fellow, IEEE)

¹Department of Computer Science, Electrical and Space Engineering, Luleå University of Technology, 97187 Luleå, Sweden

²Department of Electrical Engineering, Chalmers University of Technology, 412 58 Gothenburg, Sweden

³Nokia Mobile Networks, 02610 Espoo, Finland

⁴Department of Electronics Engineering, Chungnam National University, Daejeon 34134, South Korea

CORRESPONDING AUTHOR: E. IBRAHIM (e-mail: emad.farouk.ibrahim@ltu.se)

This work was supported in part by the European Project Hexa-X II under Grant 101095759, and in part by the European Interreg Aurora Project Arctic-6G.

ABSTRACT Polarization is a fundamental property of electromagnetic radio signals but often neglected in localization studies. In this paper, we study the potential benefits of integrating the polarization dimension into localization applications. We develop a three-dimensional (3D) geometric channel model between a base station (BS) and user equipment (UE), both equipped with dual-polarized (DP) antennas, which offers fundamental insights into the angles of departure (AoD) from the BS to the UE as well as the 3D orientation of the UE. From the model, we identify the degrees of freedom (DoF) provided by the polarization dimension for localization solutions by evaluating the rank of the equivalent Fisher information matrix. Subsequently, we leverage these DoF to introduce three distinct localization applications: (i) 3D orientation estimation, (ii) 2D AoD estimation, and (iii) mixed 2D position and 1D orientation estimation for vehicular scenarios. Furthermore, for the three localization applications we identify their regions of operation in terms of the ranges of the angles of interest, to avoid any ambiguity occurrence through the estimation process, thereby guaranteeing unique solutions. Finally, we derive the Cramér-Rao lower bounds and numerically establish the efficiency of the proposed estimators.

INDEX TERMS Polarization, localization, and 3D orientation estimation.

I. INTRODUCTION

POLARIZATION is one of the properties that characterizes electromagnetic (EM) waves. Polarization refers to the orientation of the electric field relative to the direction of propagation, and to the shape of the electric field when looking along the direction of propagation. The polarization state of an EM wave is fully characterized by two parameters: the amplitude ratio between the complex-valued vertical and horizontal components of the wave, and their relative phase difference [1]. The polarization dimension provides additional degrees of freedom (DoF) to the wireless channel beyond the long-exploited time, frequency, and space dimensions. Theoretically, the polarization dimension offers up to six possible DoF along the electric and magnetic field vectors [2]. However, due to the complexity of designing

six-port antennas, in practice, two of these DoF are typically locked up by exploiting dual-polarized (DP) antennas of two orthogonal polarizations. Over the past decades, the polarization dimension has been exploited for different technologies such as satellite communications and optical fibers [3], [4], [5]. Furthermore, the polarization dimension has been exploited in terrestrial wireless communications to provide diversity, multiplexing, and modulation using co-located DP antennas [6], [7], [8].

Radio localization is the process of identifying the geometric parameters of a specific node, such as its position, velocity, and orientation, relative to a fixed node, such as a base station. Localization has become a crucial necessity for a wide range of applications, including location-aware communications [9], autonomous

driving [10], tactile Internet [11], and unmanned aerial vehicles (UAVs). In the literature, radio localization systems have been extensively studied, spanning from satellite-based localization systems [12] to cellular network-based localization systems [13], [14]. Various positioning algorithms have been utilized, such as trilateration, triangulation, and multiple hybrid algorithms [15]. However, the polarization of EM waves has often been overlooked in most localization studies. The polarization dimension can provide additional DoF for localization, similar to its role in wireless communications, potentially leading to novel polarization-based localization solutions.

The role of polarization has been explored in a few studies within the context of radar sensing and radio localization. Radar sensing forms the first domain where the polarization of signals is exploited. A DP radar system can pre-code the polarization state of the transmitted signal and combine the received DP signals to maximize the strength of the received signal, given the polarization diversity [16], [17], [18]. Furthermore, since the target polarimetric responses vary among different targets, polarization exploitation allows for clutter suppression and target discrimination solutions. Accordingly, polarization facilitates interference mitigation techniques for target detection in clutter-based environments [19], [20]. Moreover, it allows target identification and recognition solutions by classifying the targets based on their polarization responses [21], [22]. A second domain where the polarization of signals has been exploited is radio localization. Early on, polarization has been employed with received signal strength (RSS)-based localization solutions. In [23], polarization diversity is utilized to create a monotonic distance-to-RSS relationship, enhancing the robustness of distance estimation. Additionally, [24] exploited the polarization dimension to compensate for the impact of antenna misalignment on the RSS, resulting in improved distance estimation reliability. Furthermore, there are many research works which explored the potential benefits of the polarization dimension for localization solutions based on geometric angle estimation. In [25] the directions of arrival (DoA) are estimated utilizing DP-array which improves the estimation performance given the polarization diversity. Furthermore, [26] discussed the estimation of the polarization state of the incident wave (amplitude ratio and phase difference over the DP received signal), in addition to the DoA. Thereafter, the delay is additionally estimated using either DP-array [27], [28], [29] or tri-polarized antenna array [30].

A common weakness of the aforementioned studies [25], [26], [27], [28], [29] is that predominantly assume a simplified polarization channel model. Specifically, the polarization mismatch loss that occurs in the wireless is represented by a single rotation angle in the DP received signal. However, this polarization mismatch occurs due to the three-dimensional (3D) orientation difference between the DP received waves and the DP receiver antennas [31], [32]. Hence, the simplified polarization channel models do not

capture the full richness of the information about the 3D orientations of the transmitter and/or receiver, limiting the polarization benefits to merely an additional diversity gain and restricting the potential localization solutions that address 3D orientation estimation by leveraging the rich literature on 3D polarization channel models [31], [32], [33], [34], [35], [36].

In this paper, we investigate the potential polarization solutions for localization applications operating at millimeter wave (mmwave) frequencies, where the channel is dominated by a line-of-sight (LoS) component, due to the high reflection, diffraction, and penetration losses of non-LoS (NLoS) components [37]. Our concrete contributions are as follows:

- *3D Polarization Geometric Channel Model for Localization Applications:* Considering the most simple case of a base station (BS) and user equipment (UE), both equipped with a single DP antenna, this model incorporates the 3D UE orientation and 3D UE position. It offers fundamental insights into the azimuth and elevation angles of departure (AoD) from the BS to the UE, as well as the 3D orientation of the UE. To the best of our knowledge, this is the first localization based polarization work that incorporates the UE's 3D orientation in modeling the polarization mismatch loss of the wireless channel which offers a unique perspective for novel localization solutions.
- *Localization DoF Analysis:* We identify the DoF introduced by the polarization dimension for localization solutions by evaluating the rank of the equivalent Fisher information matrix (EFIM). We demonstrate that the 3D polarization geometric channel has potential DoF that can be directly applied to localization applications. Thus, we indicate the possible geometric parameters that can be estimated by effectively exploiting the polarization dimension. Furthermore, we conduct a feasibility comparison with the scenario of using single-polarized (SP) antennas at both the transmitter and receiver. We then highlight the potential to identify new geometric channel parameters by leveraging the polarization dimension, which are not feasible with SP antennas.
- *Exemplifying Application Examples:* We present three distinct and concrete localization applications that leverage the DoF provided by the polarization dimension. In the first application, the UE estimates its 3D orientation based on prior knowledge of the AoD from the BS to the UE (e.g., from global positioning system (GPS)). In a dual, second application, we address the estimation of the AoD from the BS to the UE given prior knowledge of the UE's 3D orientation (e.g., from a gyroscope). The third application is tailored to a specific vehicular scenario, where the orientation of the vehicle UE is described by a single steering angle. In addition, the

AoD estimation provides direct information on the vehicle's 2D position, given known altitude information.

- **Performance Analysis:** For each of the three proposed localization applications, we indicate the regions of operation in terms of the range of angles that an initial acquisition step would need to ensure the absence of ambiguity. We derive the Fisher information matrix (FIM) as well as the EFIM for the proposed applications and compute the Cramér-Rao lower bounds (CRLBs) to demonstrate the efficiency of the proposed estimators.

The rest of the paper is organized as follows. Section II outlines the system and channel models. The illustration of the polarization DoF for localization solutions is presented in Section III. Section IV presents the three proposed localization applications based on the polarization DoF. In Section V, the simulation results are presented. Finally, some concluding remarks are discussed in Section VI.

Notations: In this paper, bold letters are used for vectors and matrices. The transpose, Hermitian transpose, inversion operator, and trace operator are denoted by $(\cdot)^T$, $(\cdot)^H$, $(\cdot)^{-1}$, and $\text{tr}(\cdot)$, respectively. \mathbf{x}_i and $\|\mathbf{x}\|$ denote the i -th element and the Euclidean norm of a vector \mathbf{x} , respectively. $\Re\{\cdot\}$ extracts the real part of the complex variable. $[\mathbf{X}]_{a:b,c:d}$ extracts the subset matrix along the a -th till b -th rows and the c -th till d -th columns from matrix \mathbf{X} . $|\mathcal{X}|$ denotes the cardinality of the set \mathcal{X} . \mathbf{I}_N and $\mathbf{0}_N$ denote an identity matrix of size $N \times N$ and column vector of length N with zeros entries, respectively. $\mathcal{C}_{\mathcal{N}}(\mathbf{m}, \mathbf{R})$ denotes a complex Gaussian distribution with mean vector \mathbf{m} and covariance matrix \mathbf{R} , while $U[a, b]$ denotes a continuous uniform distribution ranging from a to b .

II. SYSTEM MODEL: GEOMETRY OF THE RECEIVED POLARIZED SIGNAL

We consider the downlink channel between a BS and a UE, both equipped with a single DP antenna of vertical and horizontal polarization states along the z and y axes, respectively, as shown in Fig. 1. We will now describe the generic channel model, followed by the geometric model, and finally combine both pieces to obtain the proposed 3D polarization geometric channel model.

A. SIGNAL MODEL

We assume a narrowband single-carrier DP transmission. Thus, the received signal at the UE for the t -th transmitted symbol becomes

$$\mathbf{y}_t = \mathbf{H}\mathbf{x}_t + n_t, \quad (1)$$

where $\mathbf{x}_t \in \mathbb{C}^{2 \times 1}$ denotes the t -th transmitted symbol over the DP antenna as $\mathbf{x}_t = [x_{tv}, x_{th}]^T$, while x_{tv} and x_{th} are the transmitted signal from the vertical and horizontal antennas, respectively, such that $\mathbb{E}[\mathbf{x}_t^H \mathbf{x}_t] = P_t$ denotes the total transmitted power, $n_t \sim \mathcal{C}_{\mathcal{N}}(0, \sigma_n^2 \mathbf{I}_2)$ is the additive white Gaussian noise (AWGN) of variance σ_n^2 , and $\mathbf{H} \in \mathbb{C}^{2 \times 2}$ is the wireless channel matrix between the BS and the UE.

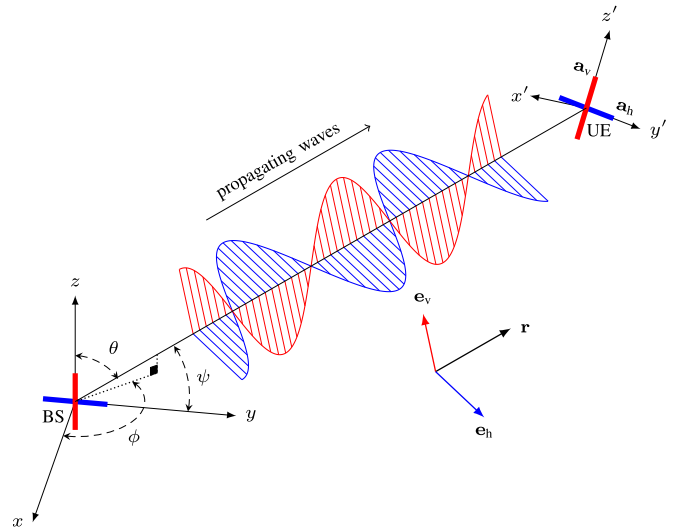


FIGURE 1. The 3D geometric channel model between a BS and a UE, each equipped with a single DP antenna.

B. GEOMETRIC CHANNEL MODEL

In this paper, we consider mmWave frequencies which typically suffer from high reflection, diffraction and penetration losses such that the channel experiences a higher proportion of LoS component in comparison to NLoS components [37]. Hence, for the sake of tractability, we restrict this work to a pure LoS environment and leave the extension to a more complex multipath as future work. A robustness analysis to multipath will be provided in Section V-D.

The polarization of an EM wave describes the orientation of the propagating EM waves relative to the direction of propagation. In LoS environment, the orientation difference between the propagating waves and the receiving antennas results in polarization mismatch loss [31]. Accordingly, when modeling the wireless channel between the BS and UE, it is crucial to identify the orientations of the propagating waves as well as those of the UE receiving antennas relative to a common reference which, without loss of generality, we choose the BS coordinate system to be. Let the BS be located at $\mathbf{p}_{BS} = [x_{BS}, y_{BS}, z_{BS}]^T$ and the UE be located in the far-field relative to the BS at $\mathbf{p}_{UE} = [x_{UE}, y_{UE}, z_{UE}]^T$. The near-field operation, which considers spherical wave propagation [38], is also possible, especially at mmWave frequencies. However, it involves a more complex channel model; therefore, it is left for future work.

1) TRANSMITTER PERSPECTIVE

The direction of the wave propagation from the BS to the UE becomes

$$\mathbf{r} = \frac{\mathbf{p}_{UE} - \mathbf{p}_{BS}}{\|\mathbf{p}_{UE} - \mathbf{p}_{BS}\|} = [\cos \phi \sin \theta, \sin \phi \sin \theta, \cos \theta]^T, \quad (2)$$

where ϕ and θ are the azimuth and elevation AoD from the BS to the UE measured relative to the z and x axes of the

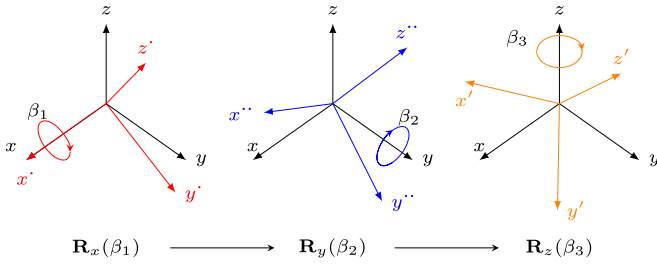


FIGURE 2. Extrinsic three-dimensional rotation model for the UE: first, the x -axis is rotated by β_1 ; then, the y -axis is rotated by β_2 ; and after that, the z -axis is rotated by β_3 .

BS, respectively, given by

$$\begin{aligned} \phi &= \tan^{-1} \left(\frac{y_{\text{UE}} - y_{\text{BS}}}{x_{\text{UE}} - x_{\text{BS}}} \right), \\ \theta &= \cos^{-1} \left(\frac{z_{\text{UE}} - z_{\text{BS}}}{\|\mathbf{p}_{\text{UE}} - \mathbf{p}_{\text{BS}}\|} \right), \end{aligned} \quad (3)$$

and shown in Fig. 1.

The BS transmits a DP signal from its vertical and horizontal antennas, which are highlighted by the red and blue waves in Fig. 1, respectively. The transmitted signal from the vertical (resp. horizontal) antenna radiates a propagating wave of an orientation vector denoted as $\mathbf{e}_v \in \mathbb{R}^{3 \times 1}$ (resp. $\mathbf{e}_h \in \mathbb{R}^{3 \times 1}$). According to the fundamentals of EM wave propagation, \mathbf{e}_v and \mathbf{e}_h are always orthogonal to the direction of wave propagation (i.e., $\mathbf{e}_v \perp \mathbf{r}$ and $\mathbf{e}_h \perp \mathbf{r}$). In addition, the orientation vector of each propagating wave belongs to the plane that is formed between the orientation vector of its particular antenna and the direction of propagation [39] (i.e., $\mathbf{e}_v \in \text{Plane}\{\mathbf{r}, \mathbf{z}\}$ and $\mathbf{e}_h \in \text{Plane}\{\mathbf{r}, \mathbf{y}\}$), where $\mathbf{y} = [0, 1, 0]^T$ and $\mathbf{z} = [0, 0, 1]^T$ denote the BS vertical and horizontal antenna orientation vectors, respectively. From these constraints, it follows (after some geometry) that [31]

$$\mathbf{e}_v = [\cos \theta \cos \phi, \cos \theta \sin \phi, -\sin \theta]^T, \quad (4)$$

$$\mathbf{e}_h = [\cot \psi \sin \theta \cos \phi, -\sin \psi, \cot \psi \cos \theta]^T, \quad (5)$$

where $\psi = \cos^{-1}(\sin \theta \sin \phi)$ represents the angle between the horizontal antenna and the direction of propagation [31], as shown in Fig. 1.

2) RECEIVER PERSPECTIVE

The orientation vectors of the receiving UE antennas reflect the orientation of the UE. We adopt a description of the UE orientation using three Euler angles [40], and we employ an extrinsic 3D rotation model shown in Fig. 2 to characterize the orientation of the UE relative to the global (BS) coordinate system. This extrinsic rotation model dictates that each rotation is performed separately and sequentially relative to the global coordinate system, starting from the x -axis followed by the y -axis and finally the z -axis.

Accordingly, the rotation matrix which accounts for the overall extrinsic rotation becomes

$$\mathbf{R}_{\text{UE}} = \mathbf{R}_z(\beta_3) \mathbf{R}_y(\beta_2) \mathbf{R}_x(\beta_1), \quad (6)$$

where $\mathbf{R}_x(\beta_1)$ denotes the rotation around the x -axis of angle β_1 , known as the roll angle, $\mathbf{R}_y(\beta_2)$ denotes the rotation around the y -axis of angle β_2 , the pitch angle, and $\mathbf{R}_z(\beta_3)$ denotes the rotation around the z -axis of angle β_3 , known as the yaw angle. The matrices $\mathbf{R}_x(\beta_1)$, $\mathbf{R}_y(\beta_2)$, and $\mathbf{R}_z(\beta_3)$ are defined in Appendix A.

Given \mathbf{R}_{UE} , the 3D rotation matrix of the UE in (6), we can identify the orientation vectors that describe the vertical and horizontal receiving antennas of the UE. Without loss of generality, the vertical and horizontal UE antennas are placed along the z and y axes of its local coordinate system, respectively. Therefore, their orientation vectors in the global coordinate system of the BS, denoted as \mathbf{a}_v and \mathbf{a}_h for the vertical and horizontal antennas, respectively, become

$$\mathbf{a}_v = \mathbf{R}_{\text{UE}} \mathbf{z}, \quad \mathbf{a}_h = \mathbf{R}_{\text{UE}} \mathbf{y}. \quad (7)$$

This description concludes the geometrical model at the receiver.

C. 3D POLARIZATION GEOMETRIC CHANNEL MODEL

After defining the orientation vectors of the propagating fields between the BS and the UE in (4)–(5) as well as those of the receiving antennas at the UE in (7), all with respect to the global BS coordinate system, the channel matrix in (1) can now be written as

$$\mathbf{H}(\theta, \phi, \beta_1, \beta_2, \beta_3) = \rho \begin{bmatrix} h_{vv} & h_{vh} \\ h_{hv} & h_{hh} \end{bmatrix} = \rho \begin{bmatrix} \mathbf{a}_v^T \mathbf{e}_v & \mathbf{a}_v^T \mathbf{e}_h \\ \mathbf{a}_h^T \mathbf{e}_v & \mathbf{a}_h^T \mathbf{e}_h \end{bmatrix}, \quad (8)$$

where $\rho = g e^{j\alpha}$ represents the complex channel gain such as $g \in \mathbb{R}$ accounts for the channel path loss, while $\alpha \in [0, 2\pi]$ accounts for the overall channel phase shift either due to the propagation delay or any mismatch at the BS or UE devices. The matrix entries in (8) describe the channel polarization mismatch losses, arising from the orientation difference between the propagating waves and the UE receiving antennas. Thus, the entries are merely the projection of the propagating fields' orientation vectors to the orientation vectors of the UE receiving antennas; i.e., $h_{ij} = \mathbf{a}_i^T \mathbf{e}_j, \forall i, j \in \{v, h\}$ [31], [32]. The wireless channel can thus be expressed as

$$\mathbf{H}(\theta, \phi, \beta_1, \beta_2, \beta_3) = g e^{j\alpha} \mathbf{A}(\beta_1, \beta_2, \beta_3) \mathbf{P}(\theta, \phi), \quad (9)$$

where $\mathbf{A}(\beta_1, \beta_2, \beta_3) = [\mathbf{a}_v, \mathbf{a}_h]^T \in \mathbb{R}^{2 \times 3}$ is a matrix that accounts for the orientation vectors of the UE antennas and $\mathbf{P}(\theta, \phi) = [\mathbf{e}_v, \mathbf{e}_h] \in \mathbb{R}^{3 \times 2}$ is a matrix that accounts for the orientations vectors of the propagating waves from the BS and the UE.

III. LOCALIZATION DEGREES OF FREEDOM

In this section, we investigate the potential DoF that can be introduced through the exploitation of the polarization domain in localization applications. It is clear that the wireless channel bears fundamental information about the geometric parameters of the UE and the BS. Specifically, the UE antenna's orientation matrix, \mathbf{A} , encapsulates information on the 3D UE orientation. On the other hand, the polarization matrix of the propagating wave, \mathbf{P} , bears information on the azimuth and elevation AoD from the BS to the UE. Consequently, the received signal at the UE conveys information on the channel parameters vector denoted as $\boldsymbol{\eta} = [\boldsymbol{\eta}_1^T, \boldsymbol{\eta}_2^T]^T$, where $\boldsymbol{\eta}_1 = [g, \alpha]^T$ and $\boldsymbol{\eta}_2 = [\theta, \phi, \beta_1, \beta_2, \beta_3]^T$ denote the nuisance and the geometric parameters of interest, respectively. The nuisance parameters refer to those parameters that are not the primary focus of localization solutions. Nevertheless, they must be estimated alongside the geometric parameters of interest, as they influence the observation models. In this paper, we assume that the nuisance parameters $\boldsymbol{\eta}_1$ are always unknown to account for any potential impairments at the BS or the UE sides. Thus, it is necessary to identify the DoF generated by exploiting the polarization domain for the estimation of the geometric parameters. In other words, indicating the number of parameters and the combination sets in $\boldsymbol{\eta}_2$ that can be estimated by exploiting the polarization domain for localization solutions.

A. DOF FROM FISHER INFORMATION

The Fisher information matrix (FIM) is a well-known tool for quantifying the performance bounds of the localization applications, which will be discussed in the next section. Additionally, the FIM can be utilized to identify the DoF of a particular estimation problem. The FIM can be computed as [41]

$$[\mathbf{I}_\eta]_{i,j} = \frac{2}{\sigma_n^2} \sum_{t=1}^T \Re \left\{ \left[\frac{\partial \boldsymbol{\mu}_t}{\partial \eta_i} \right]^H \left[\frac{\partial \boldsymbol{\mu}_t}{\partial \eta_j} \right] \right\}, \quad (10)$$

where $\boldsymbol{\mu}_t = \mathbf{H}\mathbf{x}_t$ is the noiseless received signal of (1) for the t -th transmission. The derivatives involved in the FIM are provided in Appendix B. The FIM is a symmetric matrix that incorporates both the nuisance and the geometric parameters as

$$\mathbf{I}_\eta = \begin{bmatrix} \mathbf{B} & \mathbf{C} \\ \mathbf{C}^T & \mathbf{D} \end{bmatrix}, \quad (11)$$

where $\mathbf{B} \in \mathbb{R}^{2 \times 2}$, $\mathbf{D} \in \mathbb{R}^{5 \times 5}$, and $\mathbf{C} \in \mathbb{R}^{2 \times 5}$ include the FIM derivatives of the nuisance parameters, geometric parameters, and all the parameters, respectively. To focus the Fisher information on the five geometric parameters while preserving all the necessary information, we utilize the equivalent Fisher information matrix (EFIM), defined using the Schur complement of the FIM as [42]

$$\mathbf{I}_e(\boldsymbol{\eta}_2) \triangleq \mathbf{D} - \mathbf{C}^T \mathbf{B}^{-1} \mathbf{C}. \quad (12)$$

The EFIM can be used to evaluate the DoF introduced by polarization for localization solutions. In particular, the rank of the EFIM corresponds to the number of solvable parameters in $\boldsymbol{\eta}_2$ [43], [44]. Therefore, in Appendix C, we derive a closed-form expression for the asymptotic EFIM. Subsequently, we assess its matrix rank using Gaussian elimination to reach the following proposition

Proposition 1: The rank of EFIM in (12) is at most three.

Proof: Please see Appendix C. ■

Given Proposition 1, the polarization dimension provides at most three DoF for geometric parameter estimation, where any combination set of at most three parameters out of $\boldsymbol{\eta}_2$ can be estimated given prior knowledge of the other parameters.

B. DoF FROM COUNTING

The localization problem represents the deconstructing of the wireless channel into the geometric parameters. Therefore, analyzing the channel estimation problem provides insights into the potential DoF for localization solutions. Given that the BS transmits $T \geq 2$ pilot symbols as $\mathbf{X} = [\mathbf{x}_1, \dots, \mathbf{x}_T] \in \mathbb{C}^{2 \times T}$, the UE can estimate the channel matrix, for instance, using least squares estimation as $\hat{\mathbf{H}} = \mathbf{Y}\mathbf{X}^H(\mathbf{X}\mathbf{X}^H)^{-1}$, provided that $\mathbf{X}\mathbf{X}^H$ is full rank, where $\mathbf{Y} = [\mathbf{y}_1, \dots, \mathbf{y}_T] \in \mathbb{C}^{2 \times T}$ denotes the received signal at the UE.

The entries of the channel matrix estimate provide four complex equations in the channel parameters $\boldsymbol{\eta}$. Hence, there are preliminary 8 real observations and 7 real unknowns. However, this does not imply $\boldsymbol{\eta}$ can be estimated from $\hat{\mathbf{H}}$. We observe from (9) that $\mathbf{H}e^{-j\alpha}$ is a real 2×2 matrix. So the phase of $\hat{\mathbf{H}}$ can provide an estimate of α . This leaves 4 real observations for 6 real unknowns. Consequently, only 4 of the 6 remaining channel parameters can be estimated from $\hat{\mathbf{H}}$. Thus, given that g is always assumed unknown, at most three out of the five geometric parameters in $\boldsymbol{\eta}_2$ can be identified.

C. FUNDAMENTAL LIMIT OF LOCALIZATION-BASED POLARIZATION SOLUTIONS

Based on the rank of the EFIM and the counting argument, it becomes apparent that not all the geometric parameters are jointly identifiable. In particular, the combination of at most *three unknowns out of 3D UE orientation and the AoD from the BS to UE can be estimated given the prior knowledge of the remaining two parameters*. In essence, the exploitation of the polarization dimension provides at most three DoF for the localization function in terms of geometric parameters estimation. In the next section, we consider different combinations of the three DoF introduced by polarization deployment to serve potential localization applications.

D. COMPARISON TO THE SINGLE POLARIZATION CASE

A fair comparison with the proposed setup of DP antennas at the transmitter and receiver is to consider the scenario where each of them is equipped with uniform linear arrays

(ULA) of two SP antennas. Thus, the two systems under comparison have an equal number of deployed antennas. In this scenario, the channel matrix can be formulated as

$$\mathbf{H}_{\text{SP}} = \rho_{\text{SP}} \mathbf{r}_{\text{SP}} \mathbf{t}_{\text{SP}}^{\text{H}}, \quad (13)$$

where $\rho_{\text{SP}} = g \cos(\delta) e^{j\alpha}$ is the channel gain similar to the DP case, but additionally includes the polarization mismatch loss factor denoted as $\cos(\delta) = \mathbf{a}_v^{\text{T}} \mathbf{e}_v$ arises from the orientation mismatch between the transmitter and receiver ULAs, which are assumed, without loss of generality, to have vertically polarized antennas. In addition, $\mathbf{t}_{\text{SP}} \in \mathbb{C}^{2 \times 1}$ and $\mathbf{r}_{\text{SP}} \in \mathbb{C}^{2 \times 1}$ are the transmit and receive response vectors, respectively, defined using the plane wave propagation model as [45]

$$\begin{aligned} \mathbf{t}_{\text{SP}} &= \left[1, e^{-j2\pi \Delta_t \sin(\phi_t)/\lambda} \right]^{\text{T}}, \\ \mathbf{r}_{\text{SP}} &= \left[1, e^{-j2\pi \Delta_r \sin(\phi_r)/\lambda} \right]^{\text{T}}, \end{aligned} \quad (14)$$

where λ , Δ_t , and Δ_r denote the carrier wavelength and the antenna separation distances at the transmitter and receiver ULAs, respectively, while ϕ_t and ϕ_r are the azimuth AoD and angle of arrival (AoA), respectively. In the single polarization case, the 3D orientation of the UE is coupled with the channel gain in terms of the polarization mismatch loss, *limiting the identifiable geometric parameters to merely the azimuth AoD and AoA*. This highlights the impact of utilizing DP antennas to enrich potential localization solutions compared to using ULAs with the benchmark SP antennas.

IV. POLARIZATION-AIDED LOCALIZATION APPLICATIONS

In this section, we introduce three different applications originating from exploiting the DoF of polarization in localization. The first application focuses on 3D orientation estimation, the second on 2D AoD estimation, and the third on a mixed 2D position and 1D orientation estimation for vehicular scenarios, as illustrated in Fig. 3. The relevance and use cases of each application are discussed. Then, a candidate estimator is introduced, the region of operation to avoid possible ambiguities is discussed, and the performance is quantified in terms of the CRLB. It is important to note that these applications are only feasible utilizing the polarization dimension initiated by deploying DP antennas at both the transmitter and receiver. Consequently, these problems cannot be solved when using ULA of SP antennas, as highlighted in the previous section.

A. APPLICATION A: UE ORIENTATION ESTIMATION

1) SCENARIO

In this application, the UE estimates its 3D orientation given the prior knowledge of the AoD from the BS to the UE. This scenario becomes relevant when the UE is equipped with a GPS sensor that facilitates its position estimation relative to a fixed and well-defined node, such as the BS. This problem finds applications in various domains

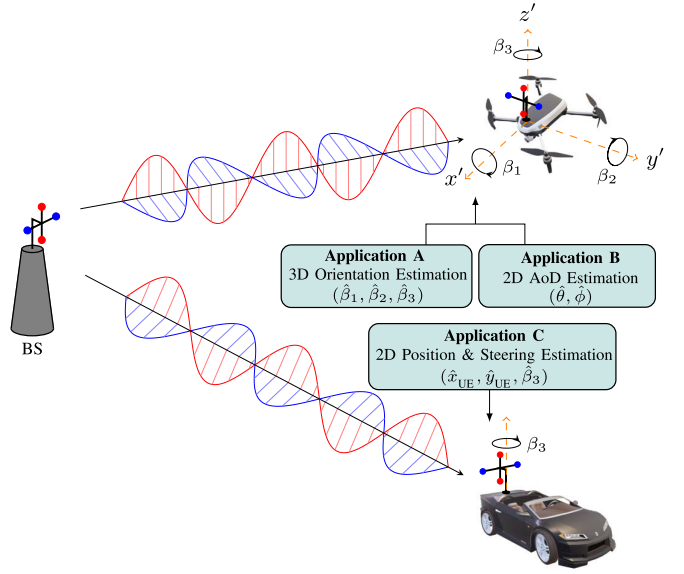


FIGURE 3. Polarization-based localization applications.

including robotics, vehicular systems, and aerial platforms, where accurate orientation estimation is crucial for ensuring successful motion and maneuvers.

2) METHOD

The unknown channel parameters to be estimated are $\boldsymbol{\eta}_a = [g, \alpha, \beta_1, \beta_2, \beta_3]^{\text{T}}$, which includes the three rotation angles of the UE as well as the amplitude and phase of the channel gain as nuisance parameters. A potential estimator for this application is as follows. First, a coarse estimation is performed using a 3D exhaustive grid search over the UE orientation angles. Then, the coarse estimates are considered as initial estimates for a gradient descent solver, such as the manifold optimization toolbox (Manopt) [46], to refine the estimates.

The maximum likelihood (ML) estimation of $\boldsymbol{\eta}_a$ is defined as

$$\hat{\boldsymbol{\eta}}_a = \arg \min_{\boldsymbol{\eta}_a} \|\mathbf{Y} - \mathbf{M}(\boldsymbol{\eta}_a)\|^2, \quad (15)$$

where $\mathbf{Y} = [\mathbf{y}_1, \dots, \mathbf{y}_T] \in \mathbb{C}^{2 \times T}$ is the received signal over T consecutive symbols and $\mathbf{M}(\boldsymbol{\eta}_a) = [\boldsymbol{\mu}_1(\boldsymbol{\eta}_a), \dots, \boldsymbol{\mu}_T(\boldsymbol{\eta}_a)]$ with $\boldsymbol{\mu}_t(\boldsymbol{\eta}_a) = \rho \mathbf{A} \mathbf{P} \mathbf{x}_t$ denotes the noiseless received signal for the t -th transmission. If the grid search estimation is utilized for (15), it will involve a search over five unknowns, resulting in prohibitive complexity. However, since the nuisance parameters, $\rho = g e^{j\alpha}$, appear linearly in the $\boldsymbol{\mu}_t(\boldsymbol{\eta}_a)$, they can be expressed in terms of the three UE orientation angles as follows. First, define $\boldsymbol{\gamma}_t(\mathbf{c}_a) = \boldsymbol{\mu}_t/\rho$, where $\mathbf{c}_a = [\beta_1, \beta_2, \beta_3]^{\text{T}}$. Then, using the least mean square estimation to express the nuisance parameters as [47]

$$\mathbf{v}(\mathbf{c}_a) = \frac{1}{T} \sum_{t=1}^T \frac{\boldsymbol{\gamma}_t^{\text{H}}(\mathbf{c}_a) \mathbf{y}_t}{\|\boldsymbol{\gamma}_t(\mathbf{c}_a)\|^2}, \quad (16)$$

where $\nu(\mathbf{c}_a)$ corresponds to the estimate of ρ when \mathbf{c}_a matches the true 3D UE orientation. Substituting $\nu(\mathbf{c}_a)$ into the ML function reduces the unknown parameters to only the three UE orientation angles as

$$\hat{\mathbf{c}}_a = \arg \min_{\mathbf{c}_a \in \mathcal{C}_a} \|\mathbf{Y} - \nu(\mathbf{c}_a)\Gamma(\mathbf{c}_a)\|^2, \quad (17)$$

where $\Gamma(\mathbf{c}_a) = [\gamma_1, \dots, \gamma_T]$, $\hat{\mathbf{c}}_a = [\hat{\beta}_1^{ini}, \hat{\beta}_2^{ini}, \hat{\beta}_3^{ini}]^T$ denotes the initial orientation angles, and \mathcal{C}_a is a set of grid points. After performing the exhaustive grid search in (17) over \mathbf{c}_a , the result is used as an initial point for a gradient descent solver to perform a refined estimation.

3) POTENTIAL AMBIGUITIES

Although, the ML function in (17) simplifies the grid search estimator to become solely over the UE orientation angles. It also may introduce unwanted ambiguity across the entire rotation angles domain. In this case, the ambiguity arises from the combined search of the nuisance parameters as a function of the orientation angles in (16). Thus, it is crucial to quantify the regions of operation in terms of UE orientation angles domains that guarantee a unique solution.

The ambiguity occurs whenever more than a single UE orientation results in a similar UE antenna orientation matrix \mathbf{A} , regardless of its sign. This occurs because the nuisance complex channel gain is estimated in terms of the UE orientation angles. Consequently, the sign of \mathbf{A} becomes indistinguishable in the ML function since $\nu(\mathbf{c}_a)$ is compensated by an excess phase shift of π in (17). The cases where ambiguity occurs for a particular UE orientation are as follows. First, the rotation around the x -axis of $\beta'_1 = \pi + \beta_1$ results in a similar but inverted UE antenna orientation matrix. Second, the extrinsic rotations around the y -axis then the z -axis of $\beta'_2 = \pi - \beta_2$ and $\beta'_3 = \beta_3 - \pi$, respectively, resulting in a similar but inverted UE antenna orientation matrix.

Thus, in this application, to avoid any potential ambiguity, we consider the region of operation for the UE orientation angles as $\beta_i \in [-\pi/2, \pi/2], \forall i \in \mathcal{I}$, where $\mathcal{I} = \{1, 2, 3\}$. This region of operation creates a feasible and broad range for various robotics, vehicular, and aerial use cases. Accordingly, the cardinality of the set \mathcal{C}_a for the grid search becomes $|\mathcal{C}_a| = (\lfloor \pi/\Delta_a \rfloor + 1)^3$, where Δ_a denotes the angle step size used in the exhaustive grid search.

4) PERFORMANCE BOUNDS

To evaluate the performance of the estimator, we rely on the CRLB for orientation angles estimation. These bounds correspond to the theoretical lower bound of the variance for any unbiased estimator. Accordingly, the EFIM for this particular application denoted as $\mathbf{I}_{e_a} = [\mathbf{I}_e]_{3:5,3:5} \in \mathbb{R}^{3 \times 3}$ is a subset matrix of the full EFIM in (12) that extracts the rows and columns corresponding to the UE orientation

angles in $\boldsymbol{\eta}_2$. Then, the orientation error bound (OEB) for this application becomes [42]

$$\text{OEB} = \sqrt{\text{tr}(\mathbf{I}_{e_a}^{-1})} \leq \sqrt{\sum_{i \in \mathcal{I}} \mathbb{E} \left[(\hat{\beta}_i - \beta_i)^2 \right]}. \quad (18)$$

B. APPLICATION B: ANGLES OF DEPARTURE ESTIMATION

1) SCENARIO

In this problem, the UE estimates the azimuth and elevation AoD from the BS to the UE given the prior knowledge of the orientation angles. This application becomes relevant and feasible when the UE is equipped with a gyroscope sensor that facilitates the accurate estimation of its orientation angles. In this scenario, the unknown channel parameters to be estimated are $\boldsymbol{\eta}_b = [g, \alpha, \theta, \phi]^T$, which include the AoD from the BS to the UE as well as the complex channel gain. The estimation of AoD has potential in many use cases as it allows the UE to detect the direction vector to the BS, relative to its local coordinate system. Additionally, the successive estimation of AoD over consecutive time instants enables the UE to infer the correct trajectory that should be tackled to reach the BS. Therefore, this application has various use cases including robotics, vehicular, and aerial domains.

2) METHOD

An estimator similar to the one used in application A can be utilized in this case. First, obtaining a coarse estimate of the azimuth and elevation AoD by employing a 2D exhaustive grid search over the AoD. Then, these coarse estimates serve as initial estimates for a gradient descent solver. The exhaustive grid search aims to maximize the likelihood function as

$$\hat{\mathbf{c}}_b = \arg \min_{\mathbf{c}_b \in \mathcal{C}_b} \|\mathbf{Y} - \nu(\mathbf{c}_b)\Gamma(\mathbf{c}_b)\|^2, \quad (19)$$

where $\nu(\mathbf{c}_b)$ and $\Gamma(\mathbf{c}_b)$ are defined similarly to application A but in terms of the initial AoD estimates denoted as $\mathbf{c}_b = [\theta, \phi]^T$, whereas \mathcal{C}_b is the set of all points in the 2D search. After that, $\hat{\mathbf{c}}_b$ is used as an initial point for a gradient descent solver to perform a refined estimation.

3) POTENTIAL AMBIGUITIES

In this application, the ambiguity occurs whenever more than a single distinct AoD results in a similar version of the propagated wave orientation matrix. Thus, given the \mathbf{P} and its orientation vector defined in (4)–(5), the ambiguity occurs whenever, $\theta' = \pi - \theta$ and $\phi' = \phi + \pi$. Thus, to avoid ambiguity we limit the region of operation for AoD estimation to $\theta \in [0, \pi]$ and $\phi \in [-\pi/2, \pi/2]$, which is a wide range for various use cases. Thus, the cardinality of the set \mathcal{C}_b for the exhaustive search becomes $|\mathcal{C}_b| = (\lfloor \pi/\Delta_b \rfloor + 1)^2$, where Δ_b denotes the angle step size employed in the exhaustive grid search.

4) PERFORMANCE BOUNDS

Moreover, the CRLB for AoD estimation can be computed using the EFIM for the unknown channel parameter η_b denoted as $\mathbf{I}_{e_b} = [\mathbf{I}_e]_{1:2,1:2} \in \mathbb{R}^{2 \times 2}$ which is a subset matrix of the full EFIM in (12) that extracts the rows and columns corresponding to azimuth and elevation AoD in η_2 . Thus, the AoD error bound (ADEB) becomes

$$\text{ADEB} = \sqrt{\text{tr}(\mathbf{I}_{e_b}^{-1})} \leq \sqrt{\mathbb{E}\left[\left(\hat{\theta} - \theta\right)^2\right] + \mathbb{E}\left[\left(\hat{\phi} - \phi\right)^2\right]}. \quad (20)$$

C. APPLICATION C: AUTONOMOUS VEHICLE LOCALIZATION

1) SCENARIO

In the previous subsections, we explored two abstract applications that can be flexibly adapted to serve various use cases and scenarios. However, in this subsection, we focus on a specific application tailored for a particular scenario. Many localization scenarios introduce constraints on the geometric channel parameters due to the characteristics of the environment and/or the specific use-case demands. For instance, in vehicular applications, assuming that streets are flat, the vehicle orientation can be fully described using the yaw angle β_3 , which corresponds to the steering angle of the vehicle. Additionally, given that the altitude of the streets in a particular geographic area is almost constant, such as z_{UE} is being known, the AoD provide information about the 2D coordinates x_{UE} and y_{UE} . Therefore, in this application, we estimate the 2D position coordinates as well as the steering angle for vehicular applications. Thus, the unknown channel parameters become $\eta_c = [g, \alpha, \theta, \phi, \beta_3]^T$.

2) METHOD

In a similar way to the preceding estimators, we conduct an exhaustive 3D grid search estimator encompassing the azimuth and elevation AoD as well as the vehicle steering angle (β_3). The exhaustive grid search aims to maximize the likelihood function as

$$\hat{\mathbf{c}}_c = \arg \min_{\mathbf{c}_c \in \mathcal{C}_c} \|\mathbf{Y} - \nu(\mathbf{c}_c)\Gamma(\mathbf{c}_c)\|^2, \quad (21)$$

where $\nu(\mathbf{c}_c)$ and $\Gamma(\mathbf{c}_c)$ are defined similarly to that in application A but in terms of $\mathbf{c}_c = [\theta, \phi, \beta_3]^T$, and \mathcal{C}_c is the set encompasses all points in the 3D exhaustive grid search. After that, $\hat{\mathbf{c}}_c$ is used as an initial point for a gradient descent solver to perform a refined estimation.

Then, the 2D coordinates of the UE can be estimated using the AoD estimates, considering that the street altitude is known which is a typical scenario in vehicular applications, as

$$\begin{aligned} \|\hat{\mathbf{r}}\| &= \frac{z_{\text{UE}} - z_{\text{BS}}}{\cos \hat{\theta}}, \\ \hat{x}_{\text{UE}} &= x_{\text{BS}} + \|\hat{\mathbf{r}}\| \sin \hat{\theta} \cos \hat{\phi}, \\ \hat{y}_{\text{UE}} &= y_{\text{BS}} + \|\hat{\mathbf{r}}\| \sin \hat{\theta} \sin \hat{\phi}. \end{aligned} \quad (22)$$

3) POTENTIAL AMBIGUITIES

In this application, the ambiguity arises during the exhaustive grid search when distinct scenarios result in a similar product between the UE antenna orientation matrix \mathbf{A} and the propagated waves orientation matrix \mathbf{P} . When considering solely the AoD, the ambiguity occurrence is similar to that in application B. While, when considering solely the steering angle there is no ambiguity. However, when considering simultaneously the AoD and steering angle, the ambiguity occurs whenever $\theta' = \pi - \theta$, $\phi' = -\phi$, and $\beta_3' = -\beta_3$. Thus, to ensure a unique solution, we define the region of operation as $\theta \in [\pi/2, \pi]$, $\phi \in [-\pi/2, \pi/2]$, and the full steering range as $\beta_3 \in [-\pi, \pi]$, which aligns well with vehicular use cases. Thus, the cardinality of \mathcal{C}_c for the grid search becomes $|\mathcal{C}_c| = (\lfloor \pi/(2\Delta_c) \rfloor + 1)(\lfloor \pi/\Delta_c \rfloor + 1)(\lfloor 2\pi/\Delta_c \rfloor + 1)$, where Δ_c denotes the angle step size used in the exhaustive grid search estimator.

4) PERFORMANCE BOUNDS

To evaluate the performance of the candidate estimator, the FIM for the state vector denoted as $s = [x_{\text{UE}}, y_{\text{UE}}, \beta_3]^T$ is needed, which can be computed as

$$\mathbf{I}_s = \mathbf{J}_s \mathbf{I}_{e_c} \mathbf{J}_s^T, \quad (23)$$

where $\mathbf{I}_{e_c} = [\mathbf{I}_e]_{(1:2,5),(1:2,5)} \in \mathbb{R}^{3 \times 3}$ represents the EFIM of the unknown channel vector which is formulated by extracting the rows and columns corresponding to η_c from the whole EFIM in (12). While $\mathbf{J}_s \in \mathbb{R}^{3 \times 3}$ is the Jacobian matrix that transforms from the channel parameter vector to the state vector which is derived in Appendix D. Accordingly, the steering error bound (SEB) and the two-dimensional UE position error bound (PEB) become

$$\begin{aligned} \text{SEB} &= \sqrt{[\mathbf{I}_s^{-1}]_{3,3}} \leq \sqrt{\mathbb{E}\left[\left(\hat{\beta}_3 - \beta_3\right)^2\right]}, \\ \text{PEB} &= \sqrt{\text{tr}\left([\mathbf{I}_s^{-1}]_{1:2,1:2}\right)} \\ &\leq \sqrt{\mathbb{E}\left[\left(\hat{x}_{\text{UE}} - x_{\text{UE}}\right)^2\right] + \mathbb{E}\left[\left(\hat{y}_{\text{UE}} - y_{\text{UE}}\right)^2\right]}. \end{aligned} \quad (24)$$

V. SIMULATION RESULTS

In this section, we present extensive numerical results to validate the DoF of the polarization dimension for localization applications, quantify the performance of the proposed estimators, study the complexity and convergence of each localization application, and discuss the impact of NLoS paths on the performances. We adopt the free space path loss model for the channel gain. In addition, the channel phase shift is randomly generated from a uniform distribution, $\alpha \sim \mathcal{U}[0, 2\pi]$. The carrier frequency is set to 30 GHz and the gain of vertical/horizontal antennas equals 3 dBi. The BS is always located at $\mathbf{p}_{\text{BS}} = [0, 0, 20]^T$ m. Moreover, the transmitted symbols from the BS over the vertical and horizontal polarization antennas are randomly generated from a quadrature phase shift keying modulation scheme.

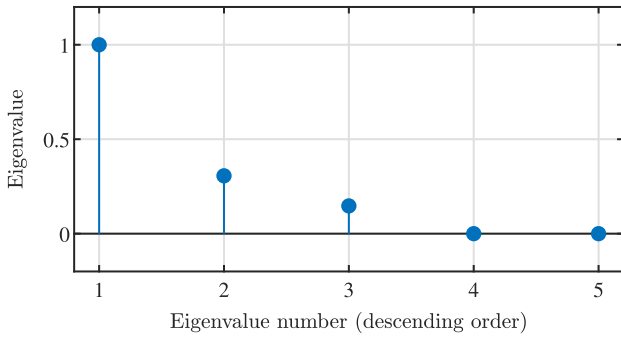


FIGURE 4. The averaged normalized eigenvalues of the EFIM, in descending order, averaged over 100,000 random realizations of the geometric channel parameters.

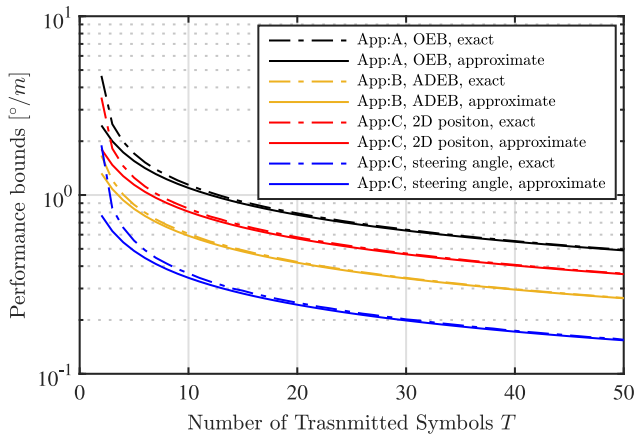


FIGURE 5. The performance bounds of the three proposed localization applications versus the number of transmitted symbols T computed using the exact and asymptotic EFIM in (12) and (47), respectively.

A. LOCALIZATION BASED POLARIZATION DoF VALIDATION

Here, we validate the three DoF introduced by the polarization dimension for localization applications as discussed in Section III and derived in Appendix C based on the rank of the EFIM. In Fig. 4, the averaged normalized eigenvalues of the EFIM, defined in (12), are plotted, setting $g = 1$, $T = 100$, and $P_t/\sigma_n^2 = 100$, using 100,000 randomly generated realizations for the azimuth and elevation AoD as well as the 3D orientation angles, which are modeled as independent uniformly distributed random variables. There are three non-zero eigenvalues, representing the rank of the EFIM. Thus, this first validates the derivation for the rank of the EFIM in Appendix C, and second, it indicates that the number of solvable parameters or combinations of the geometric parameters is three, as highlighted in the selected localization applications discussed in Section IV.

In Fig. 5, the theoretical performance bounds of the three proposed localization applications versus the number of symbols T in the processing frame are shown. The bounds are computed using the exact EFIM and the asymptotic EFIM presented in (12) and (48), respectively. The UE is located at $\mathbf{p}_{\text{UE}} = [20, 30, 1]^T$ m, and the orientation angles of the UE are $\beta_1 = 60^\circ$, $\beta_2 = 40^\circ$, and $\beta_3 = 20^\circ$. In addition,

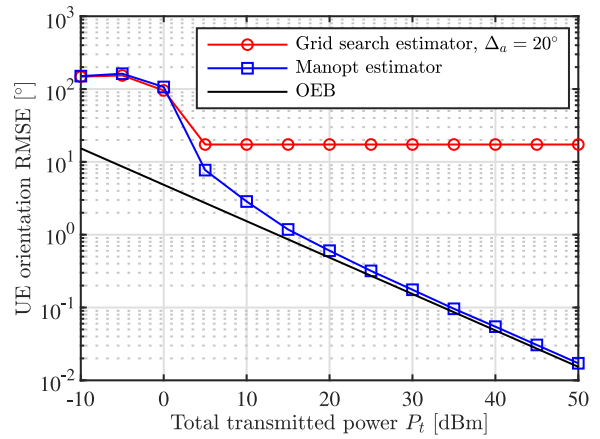


FIGURE 6. The estimation performance of application A versus the total transmitted power, given that the exhaustive grid search employs an angle step size of $\Delta_a = 20^\circ$.

the total transmitted power and the noise variance are set to $P_t = 30$ dBm and $\sigma_n^2 = -97$ dBm, respectively. It is evident that, for the three localization applications, the approximate bounds using the asymptotic EFIM converge to the exact ones with increasing the number of symbols, validating the asymptotic EFIM formula in (48).

B. PERFORMANCES OF LOCALIZATION APPLICATIONS

Here, we quantify the performance of the three localization applications proposed. In the three applications, a processing frame of $T = 500$ symbols and grid search estimators of $\Delta_a = \Delta_b = \Delta_c = 20^\circ$ are considered. In the case of applications A and B, the UE is positioned at a separation distance of $\|\mathbf{r}\| = 70$ m relative to the BS in the following direction $\theta = 50^\circ$, $\phi = 60^\circ$. In addition, the orientation angles of the UE are $\beta_1 = 60^\circ$, $\beta_2 = 40^\circ$, and $\beta_3 = 20^\circ$. On the other hand, in the case of application C, the UE (vehicle) is positioned at the following location $\mathbf{p}_{\text{UE}} = [20, 30, 1]^T$ with a steering angle of $\beta_3 = 130^\circ$ while $\beta_1 = \beta_2 = 0^\circ$ to mimic a vehicle localization scenario.

1) APPLICATION A: UE ORIENTATION ESTIMATION

In Fig. 6, the performance of application A, in terms of the estimation root mean square error (RMSE) is shown versus the total transmitted power. It is clear that the performance of the grid search estimator initially improves as the transmitted power increases. However, it eventually saturates due to the quantization error that typically occurs in grid search estimators. On the other hand, the performance of the gradient descent solver using Manopt, which uses the grid search estimates as its initial points, closely approaches the theoretical performance bound as the transmitted power increases which validates the efficiency of the candidate estimator.

2) APPLICATION B: ANGLES OF DEPARTURE ESTIMATION

In Fig. 7, the performance of application B is shown. The performance follows a similar fashion as in application A,

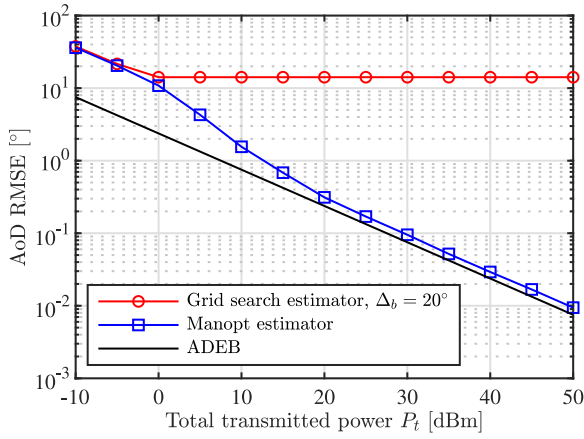


FIGURE 7. The estimation performance of application B versus the total transmitted power, given that the exhaustive grid search employs an angle step size of $\Delta_b = 20^\circ$.

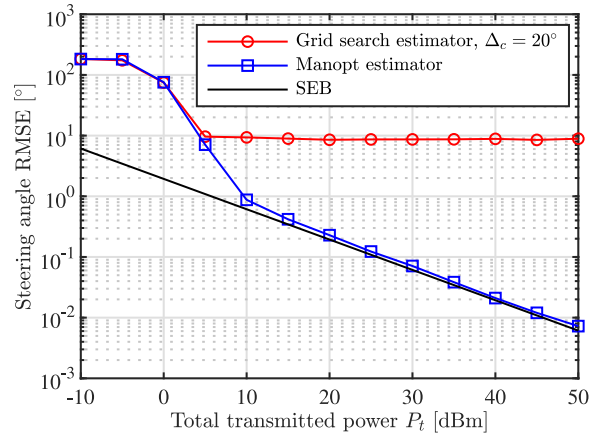


FIGURE 9. The estimation performance of steering angle for application C versus the total transmitted power, given that the exhaustive grid search employs an angle step size of $\Delta_c = 20^\circ$.

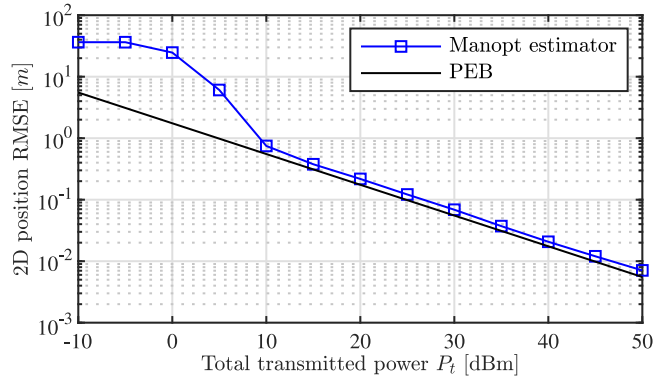


FIGURE 8. The estimation performance of vehicle 2D position for application C versus the total transmitted power, given that the exhaustive grid search employs an angle step size of $\Delta_c = 20^\circ$.

where the grid search estimator's performance reaching saturation due to quantization error and the Manopt estimator's performance aligns closely with the theoretical bound at high transmitted power, effectively confirming the efficiency of our candidate estimator.

3) APPLICATION C: AUTONOMOUS VEHICLE LOCALIZATION

In Fig. 8 and Fig. 9, the performances of the 2D position estimation and the steering angle estimation are presented, respectively. The estimations of both the 2D position and steering angle show a convergence toward the theoretical bounds at high transmitted power, affirming the potential of this application in vehicular use cases.

C. COMPLEXITY AND CONVERGENCE ANALYSIS

Here, we discuss the complexity and convergence of the two-stage estimator used in the proposed localization applications. In Fig. 10, the performance of each application versus the number of iterations employed in gradient descent solver (Manopt) is presented, at $P_t = 30$ dBm. The Manopt estimators are initialized using the grid search estimator. In

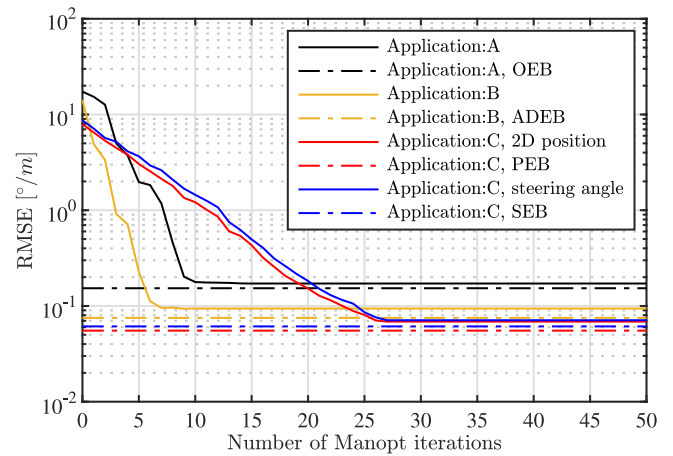


FIGURE 10. The performances of the proposed applications versus the number of iterations employed at the Manopt solver when $P_t = 30$ dBm.

the case of application B, convergence is achieved remarkably fast, within only 7 iterations, due to the optimization over a 2D manifold. However, in application A, which involves optimization over a 3D manifold, convergence is reached after 10 iterations. Application C presents additional complexity, as the solver optimizes not only over a 3D manifold but also over the product of the UE orientation and propagated wave polarization matrices, increasing the complexity. Thus, in application C, convergence is achieved after 27 iterations.

Moreover, in Fig. 11, the average running time of the estimator for each application is recorded on the same hardware platform. The running time for the grid search and the Manopt estimators is presented separately to distinguish their respective impacts on complexity. The number of iterations in the Manopt estimators is set to 7, 10, and 27 for applications A, B, and C, respectively, based on their convergence as previously indicated. The running time for application B is the lowest, as it involves a 2D grid search followed by optimization over a 2D manifold. However,

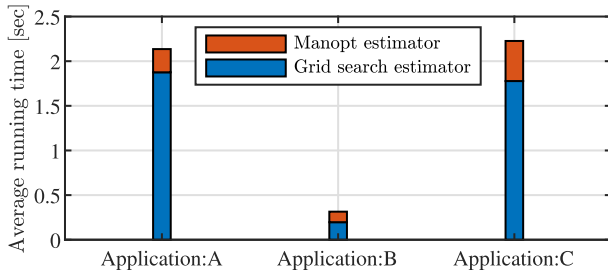


FIGURE 11. The average running time of the two stage estimator for the three proposed localization applications when $P_t = 30$ dBm.

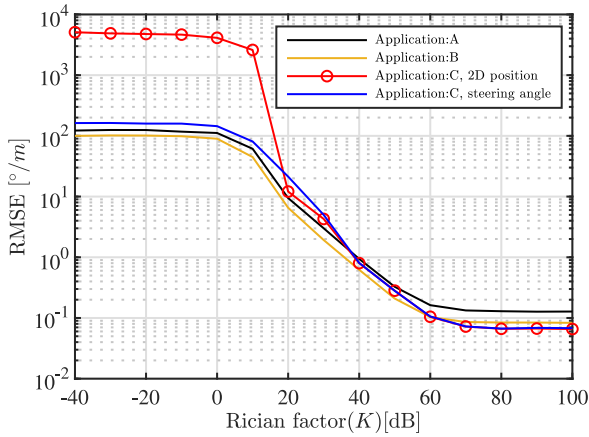


FIGURE 12. The performance of the proposed applications versus the Rician fading factor (K) when $P_t = 30$ dBm.

applications A and C involve a 3D grid search followed by optimization over 3D manifolds. Thus, the running time for application C is slightly higher than for application A due to the additional iterations required by the Manopt estimator.

D. IMPACT OF NLOS PATHS

Moreover, to assess the immunity of the proposed applications to the existence of NLoS components, in Fig. 12 we model the channel as a Rician fading channel. Then, we simulate the performances of the proposed applications versus the Rician fading factor denoted as K , at $P_t = 30$ dBm, where $K = \infty$ denotes a LoS channel and $K = 0$ denotes a Rayleigh fading channel of multipath components. As with other localization and sensing solutions, a higher proportion of LoS components compared to the unresolved NLoS components is crucial for efficient performance. Nonetheless, the proposed applications achieve acceptable performances when there is a limited portion of NLoS components in the wireless channel as the estimation performances start improving given $K \geq 20$ dB.

VI. CONCLUSION

We investigated the potential advantages of incorporating the polarization dimension for localization applications. A 3D geometric channel model between a BS and UE, both equipped with DP antennas is considered. We identified the polarization DoF for localization solutions. We introduced

three localization applications exploiting the polarization DoF. The first application enables the estimation of the UE's 3D orientation. The second application enables the estimation of the AoD from the BS to the UE. On the other hand, the third application is tailored for vehicular use cases which allows the vehicle to estimate its 2D position and the steering angle. Furthermore, for each localization application, we discussed the recommended regions of operation to prevent ambiguity occurrence in the estimation process. Moreover, we validated the efficiency of the candidate estimators by comparing the performances to the CRLBs. For future work, several developments could be explored, such as incorporating multiple DP antennas at both the transmitter and receiver. Furthermore, investigating a multipath channel model that includes both the LoS and NLoS components is crucial, as the resolved NLoS paths are expected to enhance the localization solutions by leveraging the polarization diversity provided by the polarization dimension.

APPENDIX A DEFINITION OF THE ROTATION MATRICES

$\mathbf{R}_x(\beta_1)$ denotes the rotation around the x -axis of angle β_1 , known as the roll angle, as

$$\mathbf{R}_x(\beta_1) = \begin{bmatrix} 1 & 0 & 0 \\ 0 & \cos \beta_1 & -\sin \beta_1 \\ 0 & \sin \beta_1 & \cos \beta_1 \end{bmatrix}, \quad (25)$$

$\mathbf{R}_y(\beta_2)$ denotes the rotation around the y -axis of angle β_2 , the pitch angle, as

$$\mathbf{R}_y(\beta_2) = \begin{bmatrix} \cos \beta_2 & 0 & \sin \beta_2 \\ 0 & 1 & 0 \\ -\sin \beta_2 & 0 & \cos \beta_2 \end{bmatrix}, \quad (26)$$

and $\mathbf{R}_z(\beta_3)$ denotes the rotation around the z -axis of angle β_3 , known as the yaw angle, as

$$\mathbf{R}_z(\beta_3) = \begin{bmatrix} \cos \beta_3 & -\sin \beta_3 & 0 \\ \sin \beta_3 & \cos \beta_3 & 0 \\ 0 & 0 & 1 \end{bmatrix}. \quad (27)$$

APPENDIX B GRADIENTS IN THE FISHER INFORMATION MATRIX

Here, we introduce the derivatives in (10). For the nuisance unknown complex channel gain, the derivatives can be computed as

$$\frac{\partial \boldsymbol{\mu}_t}{\partial g} = e^{j\alpha} \mathbf{A} \mathbf{P} \mathbf{x}_t, \quad (28)$$

$$\frac{\partial \boldsymbol{\mu}_t}{\partial \alpha} = j g e^{j\alpha} \mathbf{A} \mathbf{P} \mathbf{x}_t. \quad (29)$$

Furthermore, the derivatives relative to the AoD from the BS to UE become

$$\frac{\partial \boldsymbol{\mu}_t}{\partial \theta} = g e^{j\alpha} \mathbf{A} \frac{\partial \mathbf{P}}{\partial \theta} \mathbf{x}_t, \quad (30)$$

$$\frac{\partial \boldsymbol{\mu}_t}{\partial \phi} = g e^{j\alpha} \mathbf{A} \frac{\partial \mathbf{P}}{\partial \phi} \mathbf{x}_t, \quad (31)$$

where $\frac{\partial \mathbf{P}}{\partial \theta} = [\frac{\partial \mathbf{e}_v}{\partial \theta}, \frac{\partial \mathbf{e}_h}{\partial \theta}]$. Thus, using (4)–(5) we compute

$$\frac{\partial \mathbf{e}_v}{\partial \theta} = [-\sin \theta \cos \phi, -\sin \theta \sin \phi, -\cos \theta]^T, \quad (32)$$

and by utilizing $\frac{\partial \psi}{\partial \theta} = \frac{-\cos \theta \sin \phi}{\sqrt{1-\sin^2 \theta \sin^2 \phi}}$, $\frac{\partial \mathbf{e}_h}{\partial \theta}$ becomes

$$\frac{\partial \mathbf{e}_h}{\partial \theta} = \begin{bmatrix} \cos \theta \cos \phi \left(\cot \psi + \frac{\sin \theta \sin \phi \csc^2 \psi}{\sqrt{1-\sin^2 \theta \sin^2 \phi}} \right) \\ \frac{\cos \theta \sin \phi \cos \psi}{\sqrt{1-\sin^2 \theta \sin^2 \phi}} \\ -\sin \theta \cot \psi + \frac{\cos^2 \theta \sin \phi \csc^2 \psi}{\sqrt{1-\sin^2 \theta \sin^2 \phi}} \end{bmatrix}. \quad (33)$$

Similarly, $\frac{\partial \mathbf{P}}{\partial \phi} = [\frac{\partial \mathbf{e}_v}{\partial \phi}, \frac{\partial \mathbf{e}_h}{\partial \phi}]$. So,

$$\frac{\partial \mathbf{e}_v}{\partial \phi} = [-\cos \theta \sin \phi, \cos \theta \cos \phi, 0]^T, \quad (34)$$

and by utilizing $\frac{\partial \psi}{\partial \phi} = \frac{-\sin \theta \cos \phi}{\sqrt{1-\sin^2 \theta \sin^2 \phi}}$, $\frac{\partial \mathbf{e}_h}{\partial \phi}$ becomes

$$\frac{\partial \mathbf{e}_h}{\partial \phi} = \begin{bmatrix} -\sin \theta \sin \phi \cot \psi + \frac{\sin^2 \theta \cos^2 \phi \csc^2 \psi}{\sqrt{1-\sin^2 \theta \sin^2 \phi}} \\ \frac{\sin \theta \cos \phi \cos \psi}{\sqrt{1-\sin^2 \theta \sin^2 \phi}} \\ \frac{\cos \theta \sin \theta \cos \phi \csc^2 \psi}{\sqrt{1-\sin^2 \theta \sin^2 \phi}} \end{bmatrix}. \quad (35)$$

Moreover, the derivatives with respect to the three UE rotation angles can be computed as

$$\frac{\partial \boldsymbol{\mu}_i}{\partial \beta_i} = g e^{j\alpha} \frac{\partial \mathbf{A}}{\partial \beta_i} \mathbf{P} \mathbf{x}_i, \quad \forall i \in \mathcal{I} \quad (36)$$

where $\mathcal{I} = \{1, 2, 3\}$ and using $\mathbf{A} = (\mathbf{R}_{\text{UE}} \mathbf{Q})^T$ such as $\mathbf{Q} = [\mathbf{q}_1, \mathbf{q}_2] \in \mathbb{R}^{3 \times 2}$ selects the third and second columns of \mathbf{R}_{UE} . Thus, $\mathbf{Q} = [\mathbf{q}_1, \mathbf{q}_2]$ with $\mathbf{q}_1 = [0, 0, 1]^T$ and $\mathbf{q}_2 = [0, 1, 0]^T$. So, the derivatives in (36) become

$$\frac{\partial \mathbf{A}}{\partial \beta_i} = \left(\frac{\partial \mathbf{R}_{\text{UE}}}{\partial \beta_i} \mathbf{Q} \right)^T, \quad \forall i \in \mathcal{I}. \quad (37)$$

Then, the derivatives of the 3D rotation matrix are simply computed using (6) as

$$\frac{\partial \mathbf{R}_{\text{UE}}}{\partial \beta_1} = \mathbf{R}_z(\beta_3) \mathbf{R}_y(\beta_2) \frac{\partial \mathbf{R}_x(\beta_1)}{\partial \beta_1}, \quad (38)$$

$$\frac{\partial \mathbf{R}_{\text{UE}}}{\partial \beta_2} = \mathbf{R}_z(\beta_3) \frac{\partial \mathbf{R}_y(\beta_2)}{\partial \beta_2} \mathbf{R}_x(\beta_1), \quad (39)$$

$$\frac{\partial \mathbf{R}_{\text{UE}}}{\partial \beta_3} = \frac{\partial \mathbf{R}_z(\beta_3)}{\partial \beta_3} \mathbf{R}_y(\beta_2) \mathbf{R}_x(\beta_1), \quad (40)$$

and, the derivatives with respect to every rotation angle can be computed using (25)–(27) as

$$\frac{\partial \mathbf{R}_x(\beta_1)}{\partial \beta_1} = \begin{bmatrix} 0 & 0 & 0 \\ 0 & -\sin \beta_1 & -\cos \beta_1 \\ 0 & \cos \beta_1 & -\sin \beta_1 \end{bmatrix}, \quad (41)$$

$$\frac{\partial \mathbf{R}_y(\beta_2)}{\partial \beta_2} = \begin{bmatrix} -\sin \beta_2 & 0 & \cos \beta_2 \\ 0 & 0 & 0 \\ -\cos \beta_2 & 0 & -\sin \beta_2 \end{bmatrix}, \quad (42)$$

$$\frac{\partial \mathbf{R}_z(\beta_3)}{\partial \beta_3} = \begin{bmatrix} -\sin \beta_3 & -\cos \beta_3 & 0 \\ \cos \beta_3 & -\sin \beta_3 & 0 \\ 0 & 0 & 0 \end{bmatrix}. \quad (43)$$

APPENDIX C PROOF OF PROPOSITION 1

In this section, our aim is to evaluate the rank of the EFIM in (12). We start by showing an asymptotic closed form expression for the EFIM and subsequently determine its rank using Gaussian elimination. In (12), the matrix \mathbf{B} can be formulated using (10)–(11) and (28)–(29) as

$$\mathbf{B} = [\mathbf{I}\boldsymbol{\eta}]_{1:2,1:2} = \frac{2}{\sigma_n^2} \sum_{i=1}^T \Re \left\{ \begin{bmatrix} \mathbf{x}_i^H \mathbf{P}^H \mathbf{A}^H \mathbf{A} \mathbf{P} \mathbf{x}_i & j g \mathbf{x}_i^H \mathbf{P}^H \mathbf{A}^H \mathbf{A} \mathbf{P} \mathbf{x}_i \\ -j g \mathbf{x}_i^H \mathbf{P}^H \mathbf{A}^H \mathbf{A} \mathbf{P} \mathbf{x}_i & g^2 \mathbf{x}_i^H \mathbf{P}^H \mathbf{A}^H \mathbf{A} \mathbf{P} \mathbf{x}_i \end{bmatrix} \right\}, \quad (44)$$

where $\mathbf{x}_i = [x_{i_v}, x_{i_h}]^T$ with x_{i_v} and x_{i_h} generated from a particular PSK modulation scheme such as $\mathbb{E}[x_{i_v}^* x_{i_h}] = 0$. In addition, for simplicity, we consider equal transmitted power along the vertical and horizontal antennas as $\mathbb{E}[|x_{i_v}|^2] = \mathbb{E}[|x_{i_h}|^2] = P_t/2$. In this case, for a large number of transmitted symbols when $T \gg 1$, \mathbf{B} can be approximated as

$$\mathbf{B} \approx \frac{TP_t}{\sigma_n^2} \begin{bmatrix} \text{tr}\{\mathbf{P}^T \mathbf{A}^T \mathbf{A} \mathbf{P}\} & 0 \\ 0 & g^2 \text{tr}\{\mathbf{P}^T \mathbf{A}^T \mathbf{A} \mathbf{P}\} \end{bmatrix}. \quad (45)$$

Similarly, the matrix \mathbf{C}^T in (12), can be approximated using (10)–(11), (28)–(31) and (36) as

$$\mathbf{C}^T = [\mathbf{I}\boldsymbol{\eta}]_{3:7,1:2} \approx \frac{gTP_t}{\sigma_n^2} \begin{bmatrix} \text{tr}\{\frac{\partial \mathbf{P}^T}{\partial \theta} \mathbf{A}^T \mathbf{A} \mathbf{P}\} & 0 \\ \text{tr}\{\frac{\partial \mathbf{P}^T}{\partial \phi} \mathbf{A}^T \mathbf{A} \mathbf{P}\} & 0 \\ \text{tr}\{\mathbf{P}^T \frac{\partial \mathbf{A}^T}{\partial \beta_1} \mathbf{A} \mathbf{P}\} & 0 \\ \text{tr}\{\mathbf{P}^T \frac{\partial \mathbf{A}^T}{\partial \beta_2} \mathbf{A} \mathbf{P}\} & 0 \\ \text{tr}\{\mathbf{P}^T \frac{\partial \mathbf{A}^T}{\partial \beta_3} \mathbf{A} \mathbf{P}\} & 0 \end{bmatrix}, \quad (46)$$

and $\mathbf{D} = [\mathbf{I}\boldsymbol{\eta}]_{3:7,3:7}$ can be approximated as

$$[\mathbf{D}]_{i,j} \approx \frac{g^2 TP_t}{\sigma_n^2} \text{tr} \left\{ \frac{\partial(\mathbf{A} \mathbf{P})^T}{\partial \eta_{2_i}} \frac{\partial(\mathbf{A} \mathbf{P})}{\partial \eta_{2_j}} \right\}, \quad (47)$$

where $i, j = 1, \dots, 5$ and $\boldsymbol{\eta}_2 = [\theta, \phi, \beta_1, \beta_2, \beta_3]^T$, as defined previously. Thus, by substituting (45)–(47) in (12), a closed form solution for the EFIM can be formulated asymptotically as

$$[\mathbf{I}_e]_{i,j} \approx \xi f(\eta_{2_i}, \eta_{2_j}), \quad \text{where } i, j = 1, \dots, 5, \quad (48)$$

where $\xi = g^2 TP_t / \rho \sigma_n^2$ and $f(\eta_{2_i}, \eta_{2_j})$ is as shown in (49), shown at the top of the next page, with $\rho = \|\mathbf{A} \mathbf{P}\|^2$.

To derive the rank of \mathbf{I}_e we rely on the Gaussian elimination method. Thus, the first step is to null all the elements below $[\mathbf{I}_e]_{1,1}$ to have a reduced EFIM form as

$$[\mathbf{I}'_e]_{i,j} = [\mathbf{I}_e]_{i,j} - \frac{[\mathbf{I}_e]_{1,j} [\mathbf{I}_e]_{i,1}}{[\mathbf{I}_e]_{1,1}}, \quad \text{where } \begin{matrix} i = 2, \dots, 5 \\ j = 1, \dots, 5 \end{matrix}. \quad (50)$$

Then, the second step is to null all the elements below $[\mathbf{I}'_e]_{2,2}$ as

$$[\mathbf{I}''_e]_{i,j} = [\mathbf{I}'_e]_{i,j} - \frac{[\mathbf{I}'_e]_{2,j} [\mathbf{I}'_e]_{i,2}}{[\mathbf{I}'_e]_{2,2}}, \quad \text{where } \begin{matrix} i = 3, \dots, 5 \\ j = 1, \dots, 5 \end{matrix}. \quad (51)$$

$$f(\eta_{2i}, \eta_{2j}) = \varrho \text{tr} \left\{ \frac{\partial(\mathbf{AP})^T}{\partial \eta_{2i}} \frac{\partial(\mathbf{AP})}{\partial \eta_{2j}} \right\} - \text{tr} \left\{ \frac{\partial(\mathbf{AP})^T}{\partial \eta_{2i}} \mathbf{AP} \right\} \text{tr} \left\{ \frac{\partial(\mathbf{AP})^T}{\partial \eta_{2j}} \mathbf{AP} \right\}, \quad \text{where } i, j = 1, \dots, 5. \quad (49)$$

$$\mathbf{I}_{e_s}'' = \zeta \begin{bmatrix} f(\beta_1, \beta_1) (f(\theta, \theta) f(\phi, \phi) - f_{(\theta, \phi)}^2) & f(\beta_1, \beta_2) (f(\theta, \theta) - f(\phi, \phi) f_{(\theta, \phi)}^2) & f(\beta_1, \beta_3) (f(\theta, \theta) f(\phi, \phi) - f_{(\theta, \phi)}^2) \\ -f_{(\theta, \beta_1)}^2 f(\phi, \phi) - f_{(\phi, \beta_1)}^2 f(\theta, \theta) & -f_{(\theta, \beta_1)} f_{(\theta, \beta_2)} f(\phi, \phi) - f_{(\phi, \beta_1)} f_{(\phi, \beta_2)} f(\theta, \theta) & -f_{(\theta, \beta_1)} f_{(\theta, \beta_3)} f(\phi, \phi) - f_{(\phi, \beta_1)} f_{(\phi, \beta_3)} f(\theta, \theta) \\ + 2f_{(\theta, \beta_1)} f_{(\phi, \beta_1)} f(\theta, \phi) & + (f_{(\theta, \beta_1)} f_{(\phi, \beta_2)} + f_{(\theta, \beta_2)} f_{(\phi, \beta_1)}) f(\theta, \phi) & + (f_{(\theta, \beta_1)} f_{(\phi, \beta_3)} + f_{(\theta, \beta_3)} f_{(\phi, \beta_1)}) f(\theta, \phi) \\ f(\beta_1, \beta_2) (f(\theta, \theta) f(\phi, \phi) - f_{(\theta, \phi)}^2) & f(\beta_2, \beta_2) (f(\theta, \theta) f(\phi, \phi) - f_{(\theta, \phi)}^2) & f(\beta_2, \beta_3) (f(\theta, \theta) f(\phi, \phi) - f_{(\theta, \phi)}^2) \\ -f_{(\theta, \beta_1)} f_{(\theta, \beta_2)} f(\phi, \phi) - f_{(\phi, \beta_1)} f_{(\phi, \beta_2)} f(\theta, \theta) & -f_{(\theta, \beta_2)}^2 f(\phi, \phi) - f_{(\phi, \beta_2)}^2 f(\theta, \theta) & -f_{(\theta, \beta_2)} f_{(\theta, \beta_3)} f(\phi, \phi) - f_{(\phi, \beta_2)} f_{(\phi, \beta_3)} f(\theta, \theta) \\ + (f_{(\theta, \beta_1)} f_{(\phi, \beta_2)} + f_{(\theta, \beta_2)} f_{(\phi, \beta_1)}) f(\theta, \phi) & + 2f_{(\theta, \beta_2)} f_{(\phi, \beta_2)} f(\theta, \phi) & + (f_{(\theta, \beta_2)} f_{(\phi, \beta_3)} + f_{(\theta, \beta_3)} f_{(\phi, \beta_2)}) f(\theta, \phi) \\ f(\beta_1, \beta_3) (f(\theta, \theta) f(\phi, \phi) - f_{(\theta, \phi)}^2) & f(\beta_2, \beta_3) (f(\theta, \theta) f(\phi, \phi) - f_{(\theta, \phi)}^2) & f(\beta_3, \beta_3) (f(\theta, \theta) f(\phi, \phi) - f_{(\theta, \phi)}^2) \\ -f_{(\theta, \beta_1)} f_{(\theta, \beta_3)} f(\phi, \phi) - f_{(\phi, \beta_1)} f_{(\phi, \beta_3)} f(\theta, \theta) & -f_{(\theta, \beta_2)} f_{(\theta, \beta_3)} f(\phi, \phi) - f_{(\phi, \beta_2)} f_{(\phi, \beta_3)} f(\theta, \theta) & -f_{(\theta, \beta_3)}^2 f(\phi, \phi) - f_{(\phi, \beta_3)}^2 f(\theta, \theta) \\ + (f_{(\theta, \beta_1)} f_{(\phi, \beta_3)} + f_{(\theta, \beta_3)} f_{(\phi, \beta_1)}) f(\theta, \phi) & + (f_{(\theta, \beta_2)} f_{(\phi, \beta_3)} + f_{(\theta, \beta_3)} f_{(\phi, \beta_2)}) f(\theta, \phi) & + 2f_{(\theta, \beta_3)} f_{(\phi, \beta_3)} f(\theta, \phi) \end{bmatrix}, \quad (53)$$

After the two steps of Gaussian elimination, the reformulated EFIM has the following form

$$\mathbf{I}_e'' = \xi \begin{bmatrix} [\mathbf{I}_e']_{1,1} & [\mathbf{I}_e']_{1,2} & [\mathbf{I}_e']_{1,3} & [\mathbf{I}_e']_{1,4} & [\mathbf{I}_e']_{1,5} \\ 0 & [\mathbf{I}_e']_{2,2} & [\mathbf{I}_e']_{2,3} & [\mathbf{I}_e']_{2,4} & [\mathbf{I}_e']_{2,5} \\ \mathbf{0}_3 & \mathbf{0}_3 & \mathbf{I}_{e_{s1}}'' & \mathbf{I}_{e_{s2}}'' & \mathbf{I}_{e_{s3}}'' \end{bmatrix}, \quad (52)$$

where $\mathbf{I}_{e_s}'' = [\mathbf{I}_e'']_{3:5,3:5} = [\mathbf{I}_{e_{s1}}'', \mathbf{I}_{e_{s2}}'', \mathbf{I}_{e_{s3}}''] \in \mathbb{R}^{3 \times 3}$ which can be formulated using (48)–(51) as shown in (53), shown at the top of the page with $\zeta = 1/(f(\theta, \theta) f(\phi, \phi) - f_{(\theta, \phi)}^2)$. Moreover, by investigating (49) the following property can be reached

$$\frac{\partial \eta_{2j}}{\partial \eta_{2k}} f(\eta_{2i}, \eta_{2j}) = f(\eta_{2i}, \eta_{2k}) \quad \text{where } i, j, k = 1, \dots, 5. \quad (54)$$

The three rows in \mathbf{I}_{e_s}'' utilizing the property in (54) can be shown to be linear dependent as

$$\begin{aligned} [\mathbf{I}_{e_s}'']_{2,1:3} &= \frac{\partial \beta_1}{\partial \beta_2} [\mathbf{I}_{e_s}'']_{1,1:3} \\ [\mathbf{I}_{e_s}'']_{3,1:3} &= \frac{\partial \beta_1}{\partial \beta_3} [\mathbf{I}_{e_s}'']_{1,1:3}. \end{aligned} \quad (55)$$

Therefore, from the structure \mathbf{I}_e'' in (52), it is evident that the asymptotic EFIM is constructed from three independent rows, specifically the first three rows. Consequently, the rank of the asymptotic EFIM is three. Furthermore, the EFIM becomes richer as the number of transmitted symbols in the processing frame increases, indicating that the rank of the exact EFIM is at most three. Thus, the polarization dimension introduces at most three DoF for localization solutions. In other words, any combination of at most three parameters from η_2 can be estimated given prior knowledge of the other parameters.

APPENDIX D JACOBIAN MATRIX FOR APPLICATION C

Here, we derive the Jacobian matrix for FIM derivation of application C in (23). The Jacobian matrix $\mathbf{J}_s \in \mathbb{R}^{3 \times 3}$ is defined as [41]

$$[\mathbf{J}_s]_{i,j} = \frac{\partial \eta_{2,c_j}}{\partial s_i}, \quad (56)$$

where $\eta_{2,c} = [\theta, \phi, \beta_3]^T$ is the geometric channel vector of interest in application C. It is important to define the channel parameters in terms of the state vector entries. The azimuth and elevation AoD are defined in (3). Thus, the Jacobian matrix becomes

$$\mathbf{J}_s = \begin{bmatrix} \frac{\partial \theta}{\partial x_{\text{UE}}} & \frac{\partial \phi}{\partial x_{\text{UE}}} & 0 \\ \frac{\partial \theta}{\partial y_{\text{UE}}} & \frac{\partial \phi}{\partial y_{\text{UE}}} & 0 \\ 0 & 0 & 1 \end{bmatrix}. \quad (57)$$

Then, the azimuth and elevation AoD derivatives relative to the 2D position become

$$\frac{\partial \theta}{\partial x_{\text{UE}}} = \frac{\Delta x \Delta z}{\|\mathbf{r}\|^2 \sqrt{\Delta x^2 + \Delta y^2}}, \quad (58)$$

$$\frac{\partial \theta}{\partial y_{\text{UE}}} = \frac{\Delta y \Delta z}{\|\mathbf{r}\|^2 \sqrt{\Delta x^2 + \Delta y^2}}, \quad (59)$$

$$\frac{\partial \phi}{\partial x_{\text{UE}}} = \frac{-\Delta y}{\Delta x^2 + \Delta y^2}, \quad (60)$$

$$\frac{\partial \phi}{\partial y_{\text{UE}}} = \frac{\Delta x}{\Delta x^2 + \Delta y^2}. \quad (61)$$

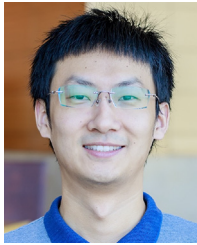
REFERENCES

- [1] C. Guo, F. Liu, S. Chen, C. Feng, and Z. Zeng, "Advances on exploiting polarization in wireless communications: Channels, technologies, and applications," *IEEE Commun. Surveys Tuts.*, vol. 19, no. 1, pp. 125–166, 1st Quart., 2017.
- [2] T. Svantesson, M. A. Jensen, and J. W. Wallace, "Analysis of electromagnetic field polarizations in multiantenna systems," *IEEE Trans. Wireless Commun.*, vol. 3, no. 2, pp. 641–646, Mar. 2004.
- [3] S. Benedetto and P. Poggiolini, "Theory of polarization shift keying modulation," *IEEE Trans. Commun.*, vol. 40, no. 4, pp. 708–721, Apr. 1992.
- [4] M. I. Hayee, M. C. Cardakli, A. B. Sahin, and A. E. Willner, "Doubling of bandwidth utilization using two orthogonal polarizations and power unbalancing in a polarization-division-multiplexing scheme," *IEEE Photon. Technol. Lett.*, vol. 13, no. 8, pp. 881–883, Aug. 2001.
- [5] M. Sellathurai, P. Guinand, and J. Lodge, "Space-time coding in mobile satellite communications using dual-polarized channels," *IEEE Trans. Veh. Technol.*, vol. 55, no. 1, pp. 188–199, Jan. 2006.
- [6] Y. Deng, A. Burr, and G. White, "Performance of MIMO systems with combined polarization multiplexing and transmit diversity," in *Proc. IEEE 61st Veh. Technol. Conf.*, vol. 2, 2005, pp. 869–873.

- [7] W. Lee and Y. Yeh, "Polarization diversity system for mobile radio," *IEEE Trans. Commun.*, vol. 20, no. 5, pp. 912–923, Oct. 1972.
- [8] B. Cao, Q.-Y. Zhang, and L. Jin, "Polarization division multiple access with polarization modulation for LOS wireless communications," *EURASIP J. Wireless Commun. Netw.*, vol. 2011, pp. 1–9, Aug. 2011.
- [9] R. Di Taranto, S. Muppirisetty, R. Raulefs, D. Slock, T. Svensson, and H. Wymeersch, "Location-aware communications for 5G networks: How location information can improve scalability, latency, and robustness of 5G," *IEEE Signal Process. Mag.*, vol. 31, no. 6, p. 112, Nov. 2014.
- [10] G. Bresson, Z. Alsayed, L. Yu, and S. Glaser, "Simultaneous localization and mapping: A survey of current trends in autonomous driving," *IEEE Trans. Intell. Veh.*, vol. 2, no. 3, pp. 194–220, Sep. 2017.
- [11] K. Antonakoglou, X. Xu, E. Steinbach, T. Mahmoodi, and M. Dohler, "Toward haptic communications over the 5G tactile Internet," *IEEE Commun. Surveys Tuts.*, vol. 20, no. 4, pp. 3034–3059, 4th Quart., 2018.
- [12] P. Enge and P. Misra, "Special issue on global positioning system," *Proc. IEEE*, vol. 87, no. 1, pp. 3–15, Jan. 1999.
- [13] M. Ibrahim and M. Youssef, "CellSense: An accurate energy-efficient GSM positioning system," *IEEE Trans. Veh. Technol.*, vol. 61, no. 1, pp. 286–296, Jan. 2012.
- [14] C. Laoudias, A. Moreira, S. Kim, S. Lee, L. Wirola, and C. Fischione, "A survey of enabling technologies for network localization, tracking, and navigation," *IEEE Commun. Surveys Tuts.*, vol. 20, no. 4, pp. 3607–3644, 4th Quart., 2018.
- [15] J. A. del Peral-Rosado, R. Raulefs, J. A. López-Salcedo, and G. Seco-Granados, "Survey of cellular mobile radio localization methods: From 1G to 5G," *IEEE Commun. Surveys Tuts.*, vol. 20, no. 2, pp. 1124–1148, 2nd Quart., 2018.
- [16] A. Kostinski and W. Boerner, "On foundations of radar polarimetry," *IEEE Trans. Antennas Propag.*, vol. 34, no. 12, pp. 1395–1404, Dec. 1986.
- [17] W.-M. Boerner and A. Kostinski, "On the concept of the polarimetric matched filter in high resolution radar imaging," in *Proc. IEEE AP-S. Int. Symp., Antennas Propagat.*, 1988, pp. 533–536.
- [18] W.-M. Boerner, A. Kostinski, and B. James, "On the concept of the polarimetric matched filter in high resolution radar imaging: An alternative for speckle radiation," in *Proc. Remote Sens. Moving Towards 21st Century*, vol. 1, 1988, pp. 69–72.
- [19] A. Kostinski and W. Boerner, "On the polarimetric contrast optimization," *IEEE Trans. Antennas Propag.*, vol. 35, no. 8, pp. 988–991, Aug. 1987.
- [20] A. Poelman, "Virtual polarisation adaptation a method of increasing the detection capability of a radar system through polarisation-vector processing," *IEE Proc. F, Commun., Radar Signal Process.*, vol. 128, no. 5, pp. 261–270, 1981.
- [21] D. A. Garren, A. C. Odom, M. K. Osborn, J. S. Goldstein, S. U. Pillai, and J. R. Guerci, "Full-polarization matched-illumination for target detection and identification," *IEEE Trans. Aerosp. Electron. Syst.*, vol. 38, no. 3, pp. 824–837, Jul. 2002.
- [22] F. Sadjadi, "Improved target classification using optimum polarimetric SAR signatures," *IEEE Trans. Aerosp. Electron. Syst.*, vol. 38, no. 1, pp. 38–49, Jan. 2002.
- [23] K. Chethan, T. Chakravarty, J. Prabha, M. G. Chandra, and P. Balamuralidhar, "Polarization diversity improves RSSI based location estimation for wireless sensor networks," in *Proc. Appl. Electromagn. Conf. (AEMC)*, 2009, pp. 1–4.
- [24] D. Polese, L. Pazzini, A. Minotti, L. Maiolo, and A. Pecora, "Compensation of the antenna polarization misalignment in the RSSI estimation," in *Proc. Int. Conf. Sens. Netw.*, vol. 2, 2014, pp. 263–267.
- [25] A. Nehorai and E. Paldi, "Vector-sensor array processing for electromagnetic source localization," *IEEE Trans. Signal Process.*, vol. 42, no. 2, pp. 376–398, Feb. 1994.
- [26] J. Li and R. T. Compton, "Two-dimensional angle and polarization estimation using the ESPRIT algorithm," *IEEE Trans. Antennas Propag.*, vol. 40, no. 5, pp. 550–555, May 1992.
- [27] J. W. Ng and A. Manikas, "Polarisation-angle-delay estimation using crossed-dipole array for DS-CDMA systems," in *Proc. 14th Int. Conf. Digit. Signal Process.*, vol. 1, 2002, pp. 259–262.
- [28] J. Picheral and F. Piqueres, "Joint angle/delay/polarization estimation by espritle method for multipath channel identification," in *Proc. 12th Eur. Signal Process. Conf.*, 2004, pp. 2179–2182.
- [29] L. Xu, H. Jiang, and R. Qin, "Joint parameter estimation of two-dimensional angle/delay/polarization for multipath channels," in *Proc. 4th IEEE Int. Conf. Circuits Syst. Commun.*, 2008, pp. 737–740.
- [30] J. He, Y. Wang, T. Shu, and T.-K. Truong, "Polarization, angle, and delay estimation for tri-polarized systems in multipath environments," *IEEE Trans. Wireless Commun.*, vol. 21, no. 8, pp. 5828–5841, Aug. 2022.
- [31] P. Chandhar, D. Danev, and E. G. Larsson, "Massive MIMO as enabler for communications with drone swarms," in *Proc. Int. Conf. Unmanned Aircr. Syst. (ICUAS)*, 2016, pp. 347–354.
- [32] P. Chandhar, D. Danev, and E. G. Larsson, "Massive MIMO for communications with drone swarms," *IEEE Trans. Wireless Commun.*, vol. 17, no. 3, pp. 1604–1629, Mar. 2018.
- [33] M. Shafi et al., "Polarized MIMO channels in 3-D: Models, measurements and mutual information," *IEEE J. Sel. Areas Commun.*, vol. 24, no. 3, pp. 514–527, Mar. 2006.
- [34] M.-T. Dao, V.-A. Nguyen, Y.-T. Im, S.-O. Park, and G. Yoon, "3D polarized channel modeling and performance comparison of MIMO antenna configurations with different polarizations," *IEEE Trans. Antennas Propag.*, vol. 59, no. 7, pp. 2672–2682, Jul. 2011.
- [35] S. Jaeckel, K. Borner, L. Thiele, and V. Jungnickel, "A geometric polarization rotation model for the 3-D spatial channel model," *IEEE Trans. Antennas Propag.*, vol. 60, no. 12, pp. 5966–5977, Dec. 2012.
- [36] S.-C. Kwon and G. L. Stuber, "Geometrical theory of channel depolarization," *IEEE Trans. Veh. Technol.*, vol. 60, no. 8, pp. 3542–3556, Oct. 2011.
- [37] M. Xiao et al., "Millimeter wave communications for future mobile networks," *IEEE J. Sel. Areas Commun.*, vol. 35, no. 9, pp. 1909–1935, Sep. 2017.
- [38] Y. Pan, C. Pan, S. Jin, and J. Wang, "RIS-aided near-field Localization and channel estimation for the terahertz system," *IEEE J. Sel. Topics Signal Process.*, vol. 17, no. 4, pp. 878–892, Jul. 2023.
- [39] C. A. Balanis, *Antenna Theory Analysis and Design*. Hoboken, NJ, USA: Wiley, 2005.
- [40] J. L. Blanco-Claraco, "A tutorial on $\mathbf{SE}(3)$ transformation parameterizations and on-manifold optimization," 2021, *arXiv:2103.15980*.
- [41] S. M. Kay, *Fundamentals of Statistical Signal Processing: Estimation Theory*. Upper Saddle River, NJ, USA: Prentice-Hall, Inc., 1993.
- [42] Y. Shen and M. Z. Win, "Fundamental limits of wideband localization—Part I: A general framework," *IEEE Trans. Inf. Theory*, vol. 56, no. 10, pp. 4956–4980, Oct. 2010.
- [43] M. C. Eisenberg and M. A. Hayashi, "Determining identifiable parameter combinations using subset profiling," *Math. Biosci.*, vol. 256, pp. 116–126, Oct. 2014.
- [44] C. Piazzola, L. Tamellini, and R. Tempone, "A note on tools for prediction under uncertainty and identifiability of SIR-like dynamical systems for epidemiology," *Math. Biosci.*, vol. 332, Feb. 2021, Art. no. 108514.
- [45] E. Björnson, J. Hoydis, and L. Sanguinetti, "Massive MIMO networks: Spectral, energy, and hardware efficiency," *Found. Trends® Signal Process.*, vol. 11, nos. 3–4, pp. 154–655, 2017.
- [46] N. Boumal, B. Mishra, P.-A. Absil, and R. Sepulchre, "Manopt, a Matlab toolbox for optimization on manifolds," *J. Mach. Learn. Res.*, vol. 15, no. 1, pp. 1455–1459, 2014.
- [47] H. Chen et al., "Modeling and analysis of OFDM-based 5G/6G localization under hardware impairments," *IEEE Trans. Wireless Commun.*, vol. 23, no. 7, pp. 7319–7333, Jul. 2024.



EMAD IBRAHIM received the B.Sc. and M.Sc. degrees in electrical engineering from Ain Shams University, Cairo, Egypt, in 2013 and 2018, respectively. He is currently pursuing the Ph.D. degree in Signal Processing with the Department of Computer Science, Electrical and Space Engineering, Luleå University of Technology, Sweden. His research interests include RIS, electromagnetic polarization, radio localization, and ISAC.



HUI CHEN (Member, IEEE) received the Ph.D. degree in electrical and computer engineering from the King Abdullah University of Science and Technology, Saudi Arabia, in 2021. He is currently a Research Specialist with the Chalmers University of Technology, Sweden. Prior to this, he was a Postdoctoral Researcher with Chalmers from 2021 to 2023, and a Senior Researcher with Technology Innovation Institute, UAE, from 2023 to 2024. His current research interests include 5G/6G radio localization and distributed ISAC.



RICKARD NILSSON received the Ph.D. degree in signal processing from the Luleå University of Technology (LTU), Sweden. With Telia Research AB, Sweden, and Stanford University, USA, he co-invented and researched a flexible broadband access method for very high-speed DSL and contributed to its standardization (VDSL1 and VDSL2). For seven years, he researched broadband access technologies in collaboration with industry and academia with the Telecommunications Research Center Vienna, Austria. In Vienna, he also lectured broadband access with the Technical University and supervised Ph.D. students. He is currently an Associate Professor with LTU, where he has founded a research group, initiated work in wireless communications, and software-defined radios. His research focuses on wireless communications, localization, and sensing, for next-generation terrestrial, and space systems.



ZI YE received the Ph.D. degree in networks, information and communications from the Polytechnic Institute of Paris, Paris, France in 2021. She is currently a Baseband Developer with Ericsson, Lund, Sweden, focusing on baseband RAN user plane control. She was a Postdoctoral Researcher with the Department of Computer Science, Electrical and Space Engineering, Luleå University of Technology, Sweden, from 2021 to 2023, focusing on 5G/6G wireless communications, RIS, radio localization and ISAC.



HENK WYMEERSCH (Fellow, IEEE) received the Ph.D. degree in electrical engineering/applied sciences from Ghent University, Belgium, in 2005. He is currently a Professor of Communication Systems with the Department of Electrical Engineering, Chalmers University of Technology, Sweden. Prior to joining Chalmers, he was a Postdoctoral Researcher with the Laboratory for Information and Decision Systems, Massachusetts Institute of Technology from 2005 until 2009. His current research interests include the convergence of communication and sensing, in a 5G and Beyond 5G context. He served as an Associate Editor for IEEE COMMUNICATION LETTERS from 2009 to 2013 and IEEE TRANSACTIONS ON COMMUNICATIONS from 2016 to 2018. He has been serving as an Associate Editor for IEEE TRANSACTIONS ON WIRELESS COMMUNICATIONS since 2013. He is currently a Senior Member of the IEEE Signal Processing Magazine Editorial Board. From 2019 to 2021, he was an IEEE Distinguished Lecturer with the Vehicular Technology Society.



REZA GHAZALIAN received the Ph.D. degree in telecommunication systems engineering from the Babol Noshirvani University of Technology, Babol, Iran, in 2017. He is currently a Senior RF Specification Engineer with Nokia Mobile Network. He was a Postdoctoral Researcher with the Department of Information and Communications Engineering, Aalto University from 2021 to 2022. His current research interests include RIS, radio localization, signal processing, and optimization.



HYOWON KIM (Member, IEEE) received the Ph.D. degree from the Department of Electronic Engineering, Hanyang University, Seoul, South Korea, in 2021. He is currently an Assistant Professor with the Department of Electronics Engineering, Chungnam National University, Daejeon, South Korea. He was a Marie Skłodowska-Curie Fellow/Postdoctoral Researcher with the Department of Electrical Engineering, Chalmers University of Technology, Sweden, from 2021 to 2023.



JAAP VAN DE BEEK (Fellow, IEEE) received the Ph.D. degree in 1998. He is a Chaired Professor of Signal Processing with the Luleå University of Technology, Sweden. After spending many years in industrial research labs, he returned to academia in 2013, where his research continues to focus on technologies and solutions in radio networks. In different roles, he has been involved in the various generations of mobile cellular communications systems. He was among those pioneering OFDM as an access scheme for cellular radio in the late nineties; he has been contributing to the specification of 3GPP's LTE standard for which he holds a number of essential patents; and today he explores the potential of reconfigurable meta surfaces for localization, sensing, and communication. Beyond physical layer research, his engagement extends to improvement of Internet access, wireless network connectivity, and cellular radio coverage in rural and remote regions. He is a recipient of the IEEE Communications Society Heinrich Hertz Award.